Applied Physics A (2019)125:543
https://doi.org/10.1007/s00339-019-2823-2

Applied Physics A
Materials Science & Processing

Structural, optical, electrochemical, and antibacterial features of ZnS nanoparticles: incorporation of Sn

R. Kumar[1] · P. Sakthivel[2] · P. Mani[1]

Received: 20 March 2019 / Accepted: 14 July 2019

Abstract
Incorporation of Sn into ZnS nanoparticles was performed by simple co-precipitation method and was analyzed for various parameters by X-ray diffraction (XRD), Transmission electron microscope (TEM), energy dispersive X-rays (EDX), scanning electron microscopy (SEM), Fourier transform infrared spectroscopy (FTIR), UV–visible spectroscopy, photoluminescence (PL) spectra, and electrochemical and antimicrobial studies. XRD results showed that there was no structural, geometrical alteration in Sn: ZnS and they remained in their cubic structure. Crystallite size was calculated using Debye–Scherrer method and it was ranged from 2 to 3 nm. UV–visible absorption intensity was increased for the increase of Sn concentration. Band-gap values were red shifted from that of the bulk ZnS value. The observed PL emission at 360 nm was due to transition of electrons from the shallow states near the conduction band to the sulfur vacancies present near the valence band in the ZnS lattice. Electrochemical analysis proved that the Sn = 4% composition showed a better electrical response. Since this composition of Sn had good electrical conductivity, the material can be useful to energy material applications. Antibacterial activity of Sn: ZnS nanoparticles was also discussed. A better antibacterial behavior was exhibited by 6% Sn-incorporated sample and this composition may be useful for biological applications.

1 Introduction

Quantum dots are referred as semiconductor nanoparticles whose size is 1–10 nm diameter and these are generally termed as zero-dimensional systems. As the particle size approaches their Bohr diameter, the optical properties begin to change due to the quantum confinement effect. It brings a great impact on the physical, electronic, and optical properties of the nanoparticles compared to bulk materials [1]. Especially miniaturization of the nanoparticles yields magical results on electronic and optical phenomena. Quantum dots find diverse applications in the display device, luminescent labels, field effect transistors, quantum light emitting diode QLED, spintronics, solar, optoelectronic device fabrication, and biomedical fields [2]. Therefore, cutting-edge studies are put forward by the research community from various wings of the world. Among the semiconductor combinations, II–VI group semiconductor compounds have immense technological importance in various applied fields of science and technology because of its possibility of tuning the bandgap wider [2]. ZnO, CdS, ZnSe, ZnS, CdTe, etc., are important II–VI semiconductors due to their excellent electronic and optical properties for luminescent and display device applications [3–5].

ZnS is identified as a first, direct band-gap semiconductor and it possesses two different kinds of structure, viz., cubic and wurtzite. Moreover ZnS offers different band-gap values for each structure, i.e., for cubic 3.7 eV and for wurtzite 3.4 eV. ZnS provides a better possibility to allow the dopant on its own host site; this adaptability induces the researchers' interest to study the various properties of ZnS while doped with different transition metal ions, rare-earth elements, etc. ZnS nanoparticles could be used as good photo catalysts due to the rapid generation of the electron-hole pairs by photo-excitation and highly negative reduction potentials of excited electrons; as conduction band position of ZnS has higher than the same for other semiconductors like TiO_2 and ZnO. Since a larger ratio of surface to volume of a catalyst would facilitate a better catalytic activity, the

✉ P. Sakthivel
sakthi1807@gmail.com; sakthivel.p@kahedu.edu.in

[1] Department of Physics, University College of Engineering—BIT Campus, Anna University, Tiruchirappalli, Tamilnadu 620024, India

[2] Department of Physics, Faculty of Engineering, Karpagam Academy of Higher Education, Coimbatore, Tamilnadu 641021, India

Published online: 23 July 2019

size-controlled synthesis of ZnS nanostructures to produce a larger ratio of surface to volume is of greater importance. ZnS offers better antioxidant activity particularly in oxide reduction power; it will be useful for bacteria and fungus [6]. Many researchers attempted to explore the characters of ZnO through Sn doping, which produced their results for the structural, optical, and electrical behavior of nanofilms and particles [7–13]. The structural and magnetic properties of Sn-doped ZnS nanopowders were studied in earlier studies [14]. They used a capping agent in the synthesis steps, and doping produced particle size larger almost more than the double time from the bulk.

Nanoparticles are widely used in antimicrobial activities. Some bacteria are more harmful to human health and some bacteria are useful in many respects. *Klebsiella pneumonia* causes pyogenic liver abscess and multidrug-resistant infections [15, 16]. *Bacillus thuringiensis* are identified as biological pesticide worldwide [17]. *Staphylococcus aureus* is a major human pathogen that causes wide range of clinical infections [18]. *Pseudomonas aureus* causes infections in fast manner [19]. *Escherichia coli* contains many pathotypes that cause a variety of diseases such as diarrhea, dysentery, urinary tract infections, and meningitis [20].

Sn compounds proven better antimicrobial and photocatalytic activities due to the large surface area and small particle size, lower band-gap energy of the nanoparticles, and the production of ROS, especially H_2O_2 on the surface of the nanoparticles that can penetrate the cell membrane and can cause damage to DNA and cellular proteins, leading to cell death [21]. Thus Sn-doped compounds produce excellent antimicrobial activities. To observe the exact nanobehavior of particles, we synthesized Sn-doped ZnS QDs without the aid of capping agents. To the best of our knowledge, very less work has been reported in the antimicrobial and electrochemical properties of Sn-doped ZnS nanoparticles. In the present work, we have presented the results for structural, morphological, elemental, optical, photoluminescence, and antibacterial characteristics of Sn-influenced ZnS nanoparticles.

2 Experimental techniques

2.1 Sample preparation

The Sn-doped ZnS QDs were prepared using the co-precipitation technique in room temperature. Zinc acetate ($Zn(CH_3COO)_2.2H_2O$), sodium sulfide (Na_2S), and Tin II chloride ($SnCl_2.2H_2O$) were used as source materials. Deionized water was served as a solvent for sample preparation. The subsequent purification process was avoided, because the AR grade chemicals with 99.9% purity purchased from M/S Merck. Zinc acetate, sodium sulfide, and tin II chloride were taken as per the stoichiometric ratio, and are dissolved in 50 ml double-distilled water individually, and stirred using magnetic stirrer until the chemicals fully dissolved. Those separate solutions were added simultaneously in a common beaker, which is kept under continuous stirring. The stirring rate was maintained at 1000 rpm and continued for the duration of 5 h. The required quantity of aqueous ammonia solution was added to fix the pH value = 9.5. After 5 h, a light brownish precipitate was retained at the bottom of the flask. For further purification of samples, the precipitate was filtered out, and washed with de-ionized water and methanol to remove any unwanted impurities when the synthesis was carried out. The end product was kept in a furnace for 7 h at 70 °C for removing the moisture content. The dried samples were taken out and pulverized using mortar for obtaining samples in powder form. This procedure was done for various composition of Sn = 0%, 2%, 4%, 6%, 8%.

2.1.1 Antibacterial assay

Antibacterial activity of Sn-doped ZnS nanoparticles was investigated through a well-diffusion method by the aid of Mueller Hinton agar media. Once the sterilization and solidification process was completed, wells were cut on the Mueller Hinton agar using cork borer. The antimicrobial activity of Sn-doped ZnS nanoparticles was studied at a different concentration of 10, 20, 30, and 40 µg/ml against the oral pathogen organisms. The results were recorded for different composition of Sn (0, 2, 4, 6, and 8%). The Gram-negative (*K. pneumonia*, *E. coli,* and *P. aureus*) and Gram-positive (*S. aureus* and *B. thuringiensis*) bacteria were taken for the study. These bacterial pathogens were swabbed onto the surface of Mueller Hinton agar plates. Wells were impregnated with the test samples of a concentration 50 mg/l, in which norfloxacin 10 µg was served as the standard. The plates were incubated for 30 min to allow the extract to diffuse into the medium. The plates were incubated at 35 °C for 24 h, and the zone size of inhibition was measured in millimeters. Each antibacterial assay was performed in triplicate and mean values were reported.

2.2 Characterization

An X-ray diffractometer was used to study the crystal structure of Sn-doped ZnS QDs. The diffracted patterns were recorded by a RigaKuC/max-2500 diffractometer using CuKa radiation at 40 kV and 30 mA from $2\theta = 0°–70°$ with a scan rate of 0.2°/min. The transmission electron microscopic study was taken by Philips—CM200 TEM with operating voltage from 20 to 200 kV. The surface morphology of the prepared QDs was recorded using scanning electron microscopy (SEM; JEOLJSM 6390). UV–visible optical absorption and transmittance studies were carried out to examine their

optical properties using a UV–visible spectrometer (Model: lambda 35, Make: Perkin Elmer) from 300 to 600 nm at room temperature. Halogen and deuterium lamps were used as sources for visible and UV radiations, respectively. The room-temperature FTIR studies were carried out by Fourier transform infrared (FTIR) spectrometer (Model: Perkin Elmer, Make: Spectrum RX I) from 400 to 4000 cm^{-1}. Pellets were prepared by mixing the nanoparticles with KBr at 1 wt%. Room-temperature photoluminescence (PL) studies were carried out (Model: Hitachi, Make: F-2500) at an excitation wavelength of 330 nm and power of 150 W from 345 to 500 nm to record the radiative recombination properties. The VersaSTAT MC electrochemical system (Princeton Applied Research, USA) was used to analyze the electrochemical properties of the nanoparticles. The measurements were performed in a three-electrode cell at room temperature in a 3.0 M NaCl solution. The niobium mesh covered with platinum was used as a counter electrode. The saturated calomel electrode (SCE) was taken as a reference electrode. The electrochemical impedance analysis was taken at the constant dc potential of 0.7 V under dark condition in the frequency range 0.1 Hz–1 MHz with an amplitude voltage of 10 mV.

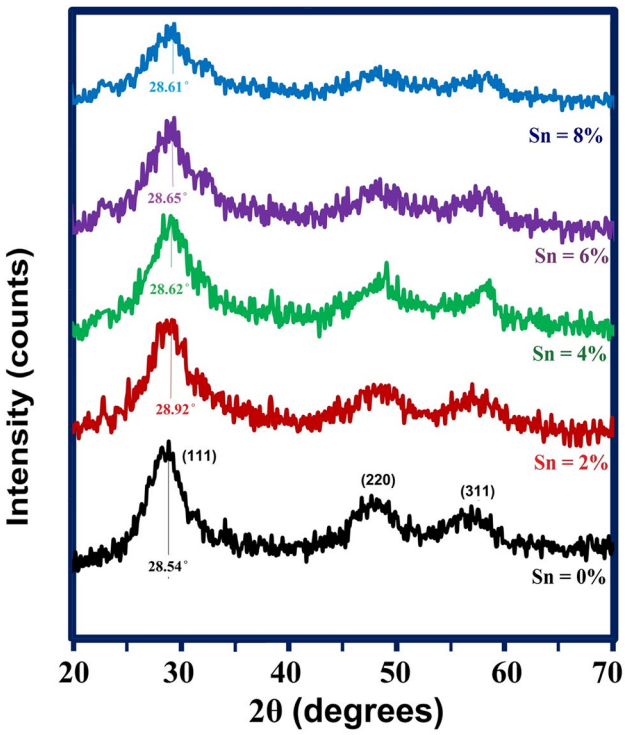

Fig. 1 XRD peaks of $Zn_{1-x}Sn_xS$ ($x = 0$, 0.02, 0.04, 0.06, & 0.08) nanoparticles

3 Results and discussion

3.1 Structural, morphological, and elemental analysis

Figure 1 shows the powder X-ray diffraction patterns of Sn-doped ZnS nanoparticles with different percentage of doping. XRD peaks were given for the range of $2\theta = 20°–70°$ with the variation of peak intensity. The crystal structure and purity were observed by the sharp high intense diffraction peaks. All the peaks corresponding to (111) (220) (311) confirmed the cubic structure of Sn-doped ZnS QDs. The primary peaks supported the JCPDS card number 05-0566. Peak intensity was reduced as the function of Sn concentration and 2θ values were shifted towards higher angle side initially for Sn 2% incorporation. Further addition of Sn concentration maintained almost the same position for primary peaks. This movement of primary peak position was attributed to the substitution of Sn into the ZnS host. A small change in the lattice parameter of ZnS host was observed and these changes were due to the variation in geometry of ions. The ionic radius of Zn^{2+} is 0.74 Å and the ionic radius of Sn is 0.99 Å [22]. During the initial substitution, distortion was produced about the dopant host. Hence, we could observe a distinct change in lattice parameter and micro-strain. This shift in peak position attributed to the alteration in crystallographic properties of the doped nanostructures owing to the difference between ionic radii. The peak positions were returned to the lower angle side by further addition of Sn concentration which may be due to the improved crystallite size. No change in the crystalline structure suggests that doping of Sn does not affect the ZnS cubic structure. The crystallite size of prepared samples was calculated using Debye–Scherrer formula [23].

$$\text{Average crystallite size } (D) = \frac{0.9\lambda}{\beta \cos\theta}, \tag{1}$$

where λ is the wavelength of X-ray in the characterization, β is the full-width at half-maximum (FWHM) intensity corresponding to (111) plane, and θ is the Bragg's diffraction angle. Micro-strain of the crystal was calculated using the formula given by the following [24]:

$$\text{Micro} - \text{strain } (\varepsilon) = \frac{\beta \cos\theta}{4}. \tag{2}$$

The peak position, FWHM value, inter-planar distance, lattice parameter, average crystallite size, and micro-strain are presented in Table 1. Crystallite size was reduced for 2% addition of the Sn and was gradually increased for further doping concentrations. Micro-strain was increased as a function of Sn-doping rate and the similar increase in micro-strain was reported for the metal-doped ZnS [25]. The decrease in crystallite size and micro-strain for the

Table 1 The peak position (2θ), full-width at half-maximum (FWHM, β) value, d value, average crystallite size (D), and micro-strain value along (111) plane of Sn-doped ZnS quantum dots

Samples	Peak position 2θ (°)	FWHM (β)	$d_{(111)}$ (Å)	Lattice parameter(a) (Å)	Crystallite size(D) (Å)	Micro-strain X 10^{-2} (ε)
ZnS	28.54	4.44	3.124	5.412	18.5	18.73
$Zn_{0.98}Sn_{0.02}S$	28.92	5.00	3.084	5.341	16.42	21.1
$Zn_{0.96}Sn_{0.04}S$	28.62	4.62	3.102	5.386	17.78	19.49
$Zn_{0.94}Sn_{0.06}S$	28.65	4.58	3.107	5.391	17.93	19.32
$Zn_{0.92}Sn_{0.08}S$	28.61	4.53	3.113	5.397	18.13	19.11

lightly doping (Sn = 2%) was due to the entry of doping atoms at grain boundaries. Extensive stress is observed for Sn 2% doping and slightly compressive stress for further addition of Sn. Calculated crystallite sizes of the present work are good agreement with 2θ values of respective peaks. For reduction in crystallite size, peak shifted to higher angle side for Sn = 2%. Further addition of Sn ions revoked the peak position towards the lower angle side.

Scanning electron microscope studies explored the surface morphology and topological features of the samples. Figure 2a, b depicts the EDX spectra of Sn-doped ZnS QDs for Sn = 0% and Sn = 2%. The EDX spectra revealed that all the taken elements were available as per the stoichiometric ratio and no other elements traced in the sample. Element versus atomic weight percentage values are made available in the same figure. The EDX spectra evidenced the purity of prepared samples and also ensured the presence of dopant.

The corresponding SEM pictures were given as inset in respective diagrams. Particle size was reduced due to Sn addition and it was obviously shown in SEM picture 2*b*. Small-sized particles appeared on the picture and it represented the presence of Sn on ZnS host. Large aggregation of small size particles on Fig. 2a and Sn addition reduced the crystallite size. Surface passivation was obtained due to Sn incorporation into ZnS host lattice because of the availability of small-sized particles.

Figure 2c represents the TEM picture of Sn (2%) doped ZnS QDs. From the analysis, we can clearly view that small-sized spherical-shaped particles are aligned like a chain in assembly of particles in Fig. 2c. The agglomeration of particles was started for further increase of Sn composition. Normally agglomeration started because of the high surface energy of nanomaterial. The surface–volume ratio of nanoparticles plays a crucial role in agglomeration process. Surface atoms may have unsaturated coordination [26]. More bonds are required to be formed by each surface atom. This attempt to make a bond tends to form a bond with neighboring particles [27]. TEM picture was given for the understanding of structural appearance of Sn-doped ZnS nanoparticles. The estimation of crystallite size was quite complex using the present TEM picture, since we could not find any isolated particles in the photograph. We can come to a conclusion that Sn 2% incorporated samples are portrayed the smaller sized particles obviously. The SEM and TEM pictures were supported the XRD results of Sn-incorporated ZnS nanoparticles.

3.2 Optical and photoluminescence studies

UV–visible absorption peaks of Sn-doped ZnS QDs for Sn = 0%, 2%, 4%, 6%, and 8% concentrations are shown in Fig. 3a. The graph was plotted from 300 to 600 nm wavelength range. Absorption peak intensity was increased with an increase of Sn concentration. A similar increase in absorption peak intensity was noticed on Sn-substituted ZnO [12]. The decreasing arm of UV absorption peaks gradually moved to higher wavelength side as the function of Sn incorporation. Sn 6% doped ZnS nanoparticles have maximum redshift in respective peak position from 303 to 310 nm. This redshift was exhibited for increase of the Sn-doping ratio and was ascribed to the Moss–Burstein effect [28]. Therefore, increasing the Sn-doping concentration made an overlapping of the Fermi energy level with the conduction band. The shifting in the position of peaks is due to doping and the change in intensity is because of the creation of defects with respect to the concentration rate of doping.

Figure 3b illustrates the transmittance characteristics of Sn-doped ZnS QDs. For the lower wavelength side, all the transmittance peak intensities were suppressed from the pure ZnS result. These results lucidly explained the light absorbing capability of samples in the UV region effectively. On the increase of wavelength, the transmittance peak intensity for all the samples was gradually enhanced. The transmittance characters of Sn-doped samples increase on visible region. This behavior will help to develop the coloring effect by absorbing UV light. Visible imaging and labeling process seek these kinds of materials for its fabrication.

The optical band-gap values of Sn-doped ZnS QDs were estimated using Tauc's relation [29]:

$$\alpha h\upsilon = A\left(h\upsilon - E_g\right)^n, \tag{3}$$

where A is a constant and E_g is an optical bandgap of the material. In the present study, the exponent 'n' is taken as ½, since it is direct allowed transitions. The bandgap (E_g)

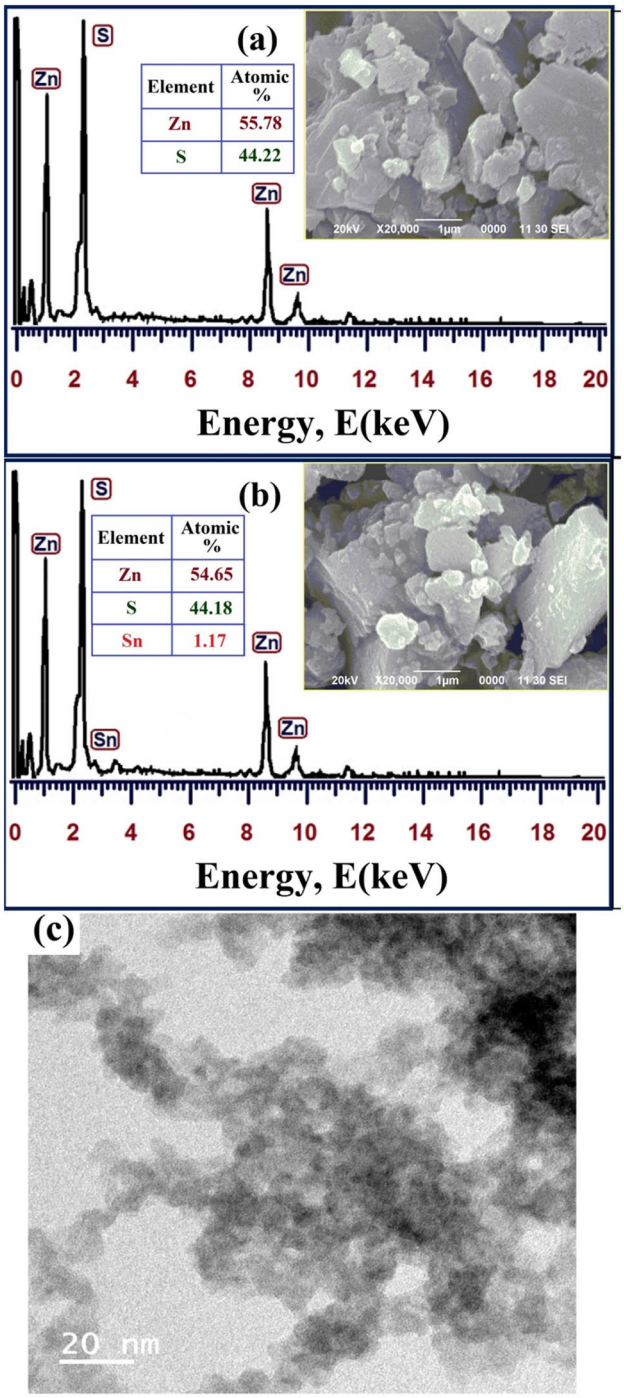

Fig. 2 **a** EDX spectra and SEM picture of ZnS nanoparticles. **b** EDX spectra and SEM picture of ZnS nanoparticles with Sn 2% doped. **c** TEM picture of 2% Sn-doped ZnS nanoparticles

can be obtained by plotting a graph $(\alpha h\upsilon)^2$ versus $h\upsilon$ and extrapolating a linear portion of the absorption edge. The calculated bandgap by Tauc's plot for all the samples is shown in Fig. 3c. Optical band energy gap values were gradually reduced as the function of Sn content. The shrinkage of bandgap was attributed to spin–spin exchange interaction made from band electrons to *d* electrons of the doped ion. Though the particle size was reduced from that of pure ZnS nanoparticles, the band-gap values got truncated. In general, quantum confinement effect plays a major role in optical band-gap tuning. However, the produced result in the present work was overcome the quantum confinement effect. It can be observed due to the variation of micro-stain, crystalline size alteration, the presence of defects, and surface ion migration [30]. These parameters might be dominated the quantum confinement effect, and thus the contraction was observed in the optical bandgap. This behavior is due to the result of a large increase in the free carrier concentration during Sn doping and the corresponding Fermi level is shifting downward to below the band edge [31]. Mass action law states that the number of particles of each type as well as the overall number of the particles must conserve whatever is their distribution on the available energy levels. To obey the mass action law and to fulfill the overall electrical charge, the Fermi level has to move away from the mid-gap position. It has to shift towards conduction band in an *n*-type semiconductor where the number of electrons *n* is higher than the number of holes ($n > p$). It shifts towards valence band in a *p*-type semiconductor where the number of electrons *n* is lower than the number of holes ($n < p$). The blocking of the low-energy transitions is known as the Burstein–Moss (BM) effect and enhances the optical gap by the energy:

$$\Delta E_g = \frac{\hbar^2 k_F^2}{2}\left[\frac{1}{m_e} + \frac{1}{m_h}\right], \tag{4}$$

where k_F is the Fermi wave vector, and m_h is the effective mass for holes in the valence band. Doping of other element produced an effect of blocking the lowest states in the conduction band, so that the optical gap is widened by a Burstein–Moss. Band-gap narrowing was caused by the correlated motion of the charge carriers and by their scattering against ionized impurities. However, the increase of carrier concentration can also cause degeneration in semiconductors. The degeneration of carriers in semiconductor can lead to opposite effects to Moss–Burstein effect. Electron and impurity (Sn) interaction is the another reason for the decrease of energy gap [32]. The schematic of bandgap is shown in Fig. 3d.

The PL spectrum of Sn-doped ZnS is shown in Fig. 4. The comparative diagram of the 0–8% Sn-doped in the Sn-ZnS lattice UV emission peaks near 360 nm. Sn doping reduced the peak intensity from the intensity value possessed by the pure ZnS QDs. Peaks were slightly red shifted for the increase of Sn doping. UV emission peak centered on 360 nm arises from the recombination of free excitons through an exciton–exciton collision process and corresponds to the near-band-edge (NBE) emission [33]. Better crystal quality is also ascribed for the strong emission in UV

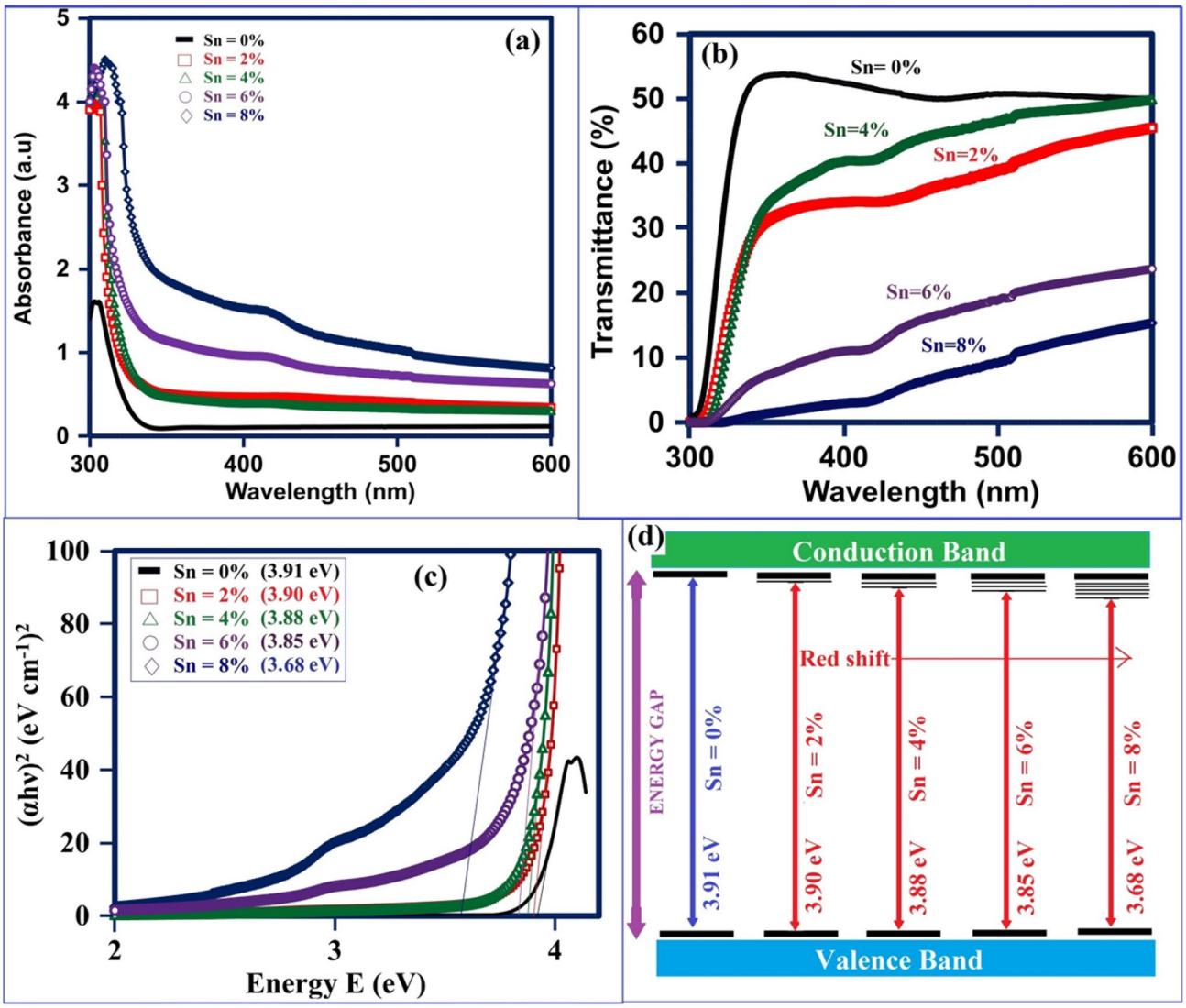

Fig. 3 **a** UV–visible absorption spectra of $Zn_{1-x}Sn_xS$ ($x=0$, 0.02, 0.04, 0.06 & 0.08) nanoparticles. **b** UV–visible transmittance spectra of $Zn_{1-x}Sn_xS$ ($x=0$, 0.02, 0.04, 0.06 & 0.08) nanoparticles. **c** The $(\alpha hv)^2$ versus hv plots of $Zn_{1-x}Sn_xS$ ($x=0$, 0.02, 0.04, 0.06 & 0.08) nanoparticles for band-gap calculation. **d** Schematic of band-gap variation of Sn-incorporated ZnS nanoparticles

region. FWHM values of PL emission peaks are decreased for Sn incorporation and the reduction was ascertained to timely construction of new recombination centers during Sn substitution. Sn 2% doped samples produced emission peak at 358 nm and further addition of Sn shifted slightly to 360 nm. This is a small redshift produced due to addition of Sn. Sn ion was substituted in ZnS host and shares sulfur with Zn [34]. This shift may also be due to the contraction of bandgap and increasing carrier concentration. Moreover the red shift of UV emission can be explained by the doping induced band-gap renormalization [35]. PL spectra will also depend on the dopant adding, related morphology, and size of the nanoparticles.

3.3 FTIR study

The FTIR analysis is used to identify the elements present in samples by tracing the molecular vibrations produced by the components of the specimens. Figure 5a depicts FTIR transmittance peaks of Sn-doped ZnS QDS from 400 to 4000 cm^{-1}. Peaks obtained near 3405 cm^{-1} were attributed to normal polymeric O–H stretching vibrations due to the presence of water molecules made available on the surface of nanocrystal [36]. Due to H–O–H bending vibrations, peaks were observed near 1606 cm^{-1} due to water molecules [37]. C–H-bending vibrations produced peaks near 1406 cm^{-1} and 1340 cm^{-1} [38]. Peaks observed around 1025 cm^{-1} were owing to the formation of microstructure

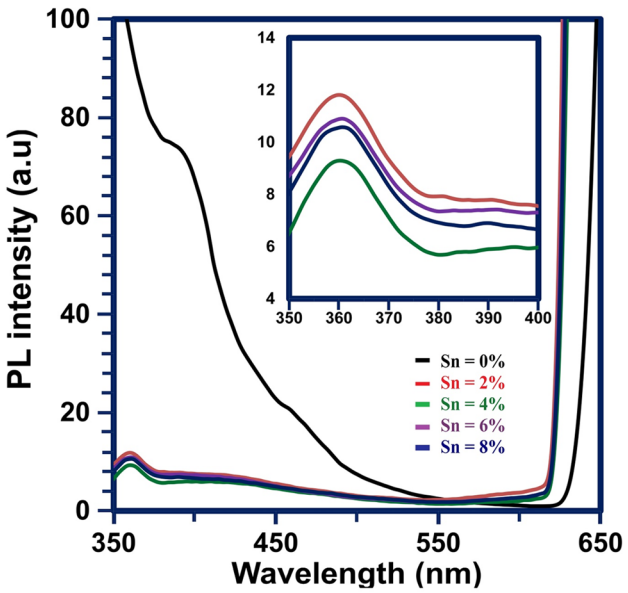

Fig. 4 Photoluminescence spectra of $Zn_{1-x}Sn_xS$ ($x=0$, 0.02, 0.04, 0.06 & 0.08) nanoparticles

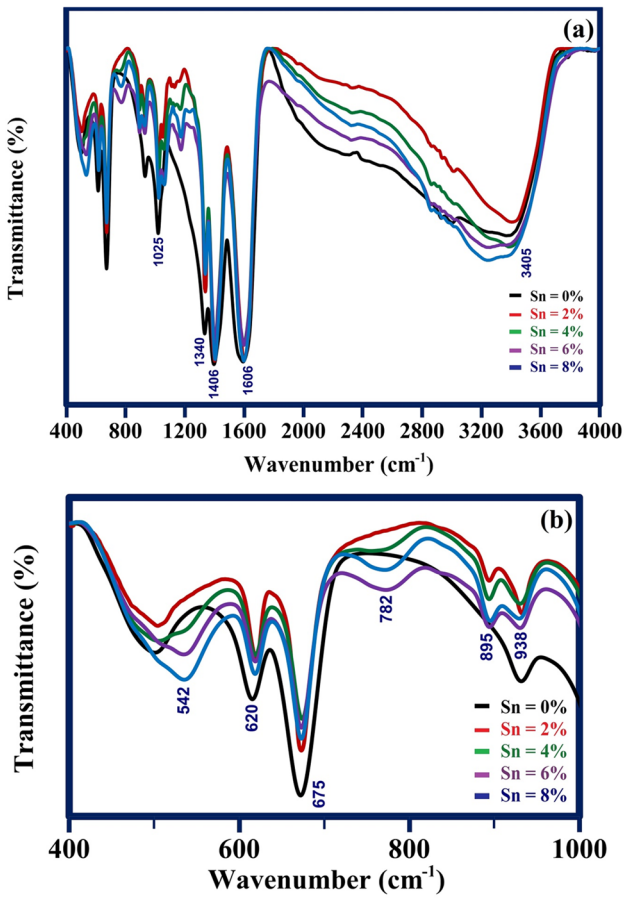

Fig. 5 **a** FTIR spectra of $Zn_{1-x}Sn_xS$ ($x=0$, 0.02, 0.04, 0.06 & 0.08) nanoparticles within the range of 400 cm^{-1} to 4000 cm^{-1}. **b** FTIR spectra of $Zn_{1-x}Sn_xS$ ($x=0$, 0.02, 0.04, 0.06 & 0.08) nanoparticles within the range of 400 cm^{-1} to 1000 cm^{-1}

in samples. Peaks received around 1200 cm^{-1} were C–O stretching in Sn-incorporated samples exclusively. Figure 5b illustrates an enlarged view of the FTIR spectra of Sn-doped ZnS QDs from 400 to 1000 cm^{-1}. The shifting of peaks from 500 to 542 cm^{-1} due to distortion produced when doping of Sn. Emission peaks identified 620 cm^{-1}, 675 cm^{-1} were due to the formation of microstructures in Zn + Sn + S ions [11]. Additional weak peaks were observed at 782 cm^{-1} and 895 cm^{-1} due to C–H bending in Sn-incorporated ZnS nanoparticles. These arrivals of additional peaks, variation of position, and peak intensity confirmed the presence of Sn ions in prepared samples. Transmittance intensity values were elevated for Sn = 2% doped sample. Higher transmittance may arise due to bonds present in the materials to absorb the incident energy. Small shifting in peaks position was observed from 400 to 1600 cm^{-1}. These minor shifting and variations are ascertained to the doping concentration. Sn 2% incorporated sample was small in size compared with others and better crystalline quality than higher percentage doping of Sn.

3.4 Electrochemical analysis

Cyclic voltammetry (CV) study is used to measure the current developed in an electrochemical cell under where the voltage was exceeded the predicted value by the Nernst equation. CV characteristics are received by cycling the potential of a working electrode and measuring the resulting current. The cyclic voltammograms for Sn-doped ZnS nanoparticles are reported in Fig. 6. The (J_{pc}) cathodic current density and (J_{pa}) anodic current density are considered as important parameters in this study. The high (J_{pc}) current peak value was received for Sn = 4% doped ZnS quantum dots. The elevated peaks were noticed either in positive and negative current values for Sn = 4%. ΔE_P is denoted as peak to peak separation. The value of ΔE_P is calculated by [39] the given formula and presented in Table 2:

$$\Delta E_P = E_{pc} - E_{pa}. \tag{5}$$

The crystalline nature of the materials with low resistivity indicates the fast charge transfer kinetics. From Table 2, it was noted that Sn 2% incorporated ZnS nanomaterials offered low ΔE_P value. This low ΔE_P values deduced an enhanced catalytic activity [40].

The Nyquist plots were plotted for the samples used in this work and they were presented in Fig. 7. From the analysis, the diameter of the semi-circle was observed more for Sn = 2% and it was further moved towards a very high-frequency side. The semi-circle area of Sn = 4%, 6%, and 8% was decreased than 2% incorporation of Sn in ZnS. Moreover, the center point of the semi-circle corresponding to Mg = 2% shifted more on the lower frequency region. The semi-circle belongs to high frequency which was represented

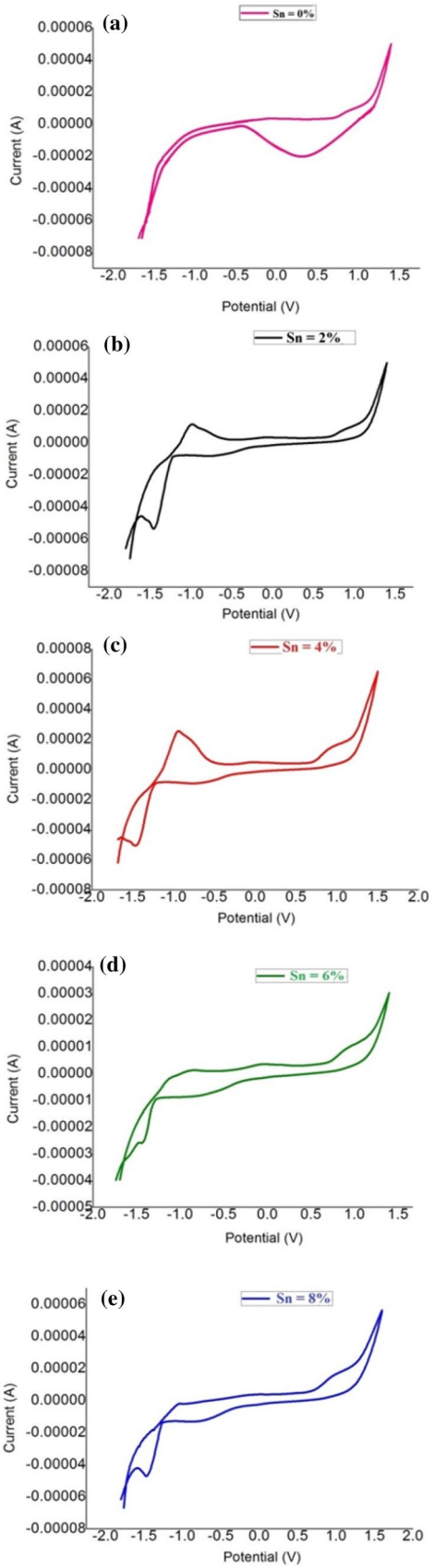

Fig. 6 Potential vs current characteristics of Sn:ZnS nanoparticles

Table 2 The ΔE_P, R_s, and R_{ct} values of Sn-doped ZnS nanoparticles

Samples	ΔE_P mV	R_s KΩ	R_{ct} KΩ
ZnS	383.2	0.096	5.692
$Zn_{0.98}Sn_{0.02}S$	179.3	−0.083	5.784
$Zn_{0.96}Sn_{0.04}S$	222.7	0.091	3.115
$Zn_{0.94}Sn_{0.06}S$	421.7	−0.181	5.350
$Zn_{0.92}Sn_{0.08}S$	237.8	0.129	3.326

as the charge transfer resistance (R_{ct}). The intercept on the real axis at high frequency was denoted as series resistance (R_s) [41]. The calculated R_S and R_{ct} values are also presented in Table 2. It was observed that from the table, the R_S and R_{ct} values of Sn = 4% lower than Sn = 0, 2, 6, and 8%. Since the low resistance was observed on Sn = 4% doped ZnS nanoparticles, this composition delivered efficient electrical property.

3.5 Antibacterial analysis

ZnS nanoparticles were used to create biologically reactive oxygen species like superoxide anions, hydroxyl radicals, and hydroxyl ions. These species provides antibacterial behavior by targeting cytoplasmic organism [42]. Sn ions produced toxicity to eradicate *S. aureus* (Gram-positive) and *Pseudomonas aeruginosa* (Gram-negative) bacterial infection [43]. An attempt was made to investigate an antibacterial activity of the combination of Sn ions with ZnS QDs. A comparative antibacterial analysis of Sn-doped ZnS QDs is shown in Fig. 8. For this comparison, we have taken five different bacteria named as a, b, c, d, e. where 'a' is *K. pneumonia*, 'b' is *E. coli*, 'c' is *B. thuringiensis*, 'd' is *S. aureus,* and 'e' is *P. aureus*. From the figure, it was noted that maximum inhibition was observed for Sn = 6% in *K. pneumonia*, *B. thuringiensis*, *S. aureus,* and *P. aureus*. Pure ZnS nanoparticles exhibited higher inhibition on *E. coli* [6]. The ZOI of pure ZnS (20 mm) is almost smaller than the standard drug for *E. coli* erythromycin (26 mm). Since the size of ZnS nanoparticles is smaller, it can easily catch the cell of bacterium via pass through the wall. The destruction of cell is easily possible which leads death of bacterium cell [44]. The electrostatic interactions of nanomaterials with bacterium cell wall and photocatalytical light activation are also considered as possible reasons for the antibacterial activities of nanomaterials [45]. For the larger ZOI of nanoparticles, larger UV absorption and emission nature are taken for deliberation. Table 3 explicitly shows the inhibition rate of various bacteria with respect to Sn-doping concentration. Since Sn-doped ZnS nanoparticles exhibited better antibacterial activity, these can be used as an antibacterial agent like food packaging industries.

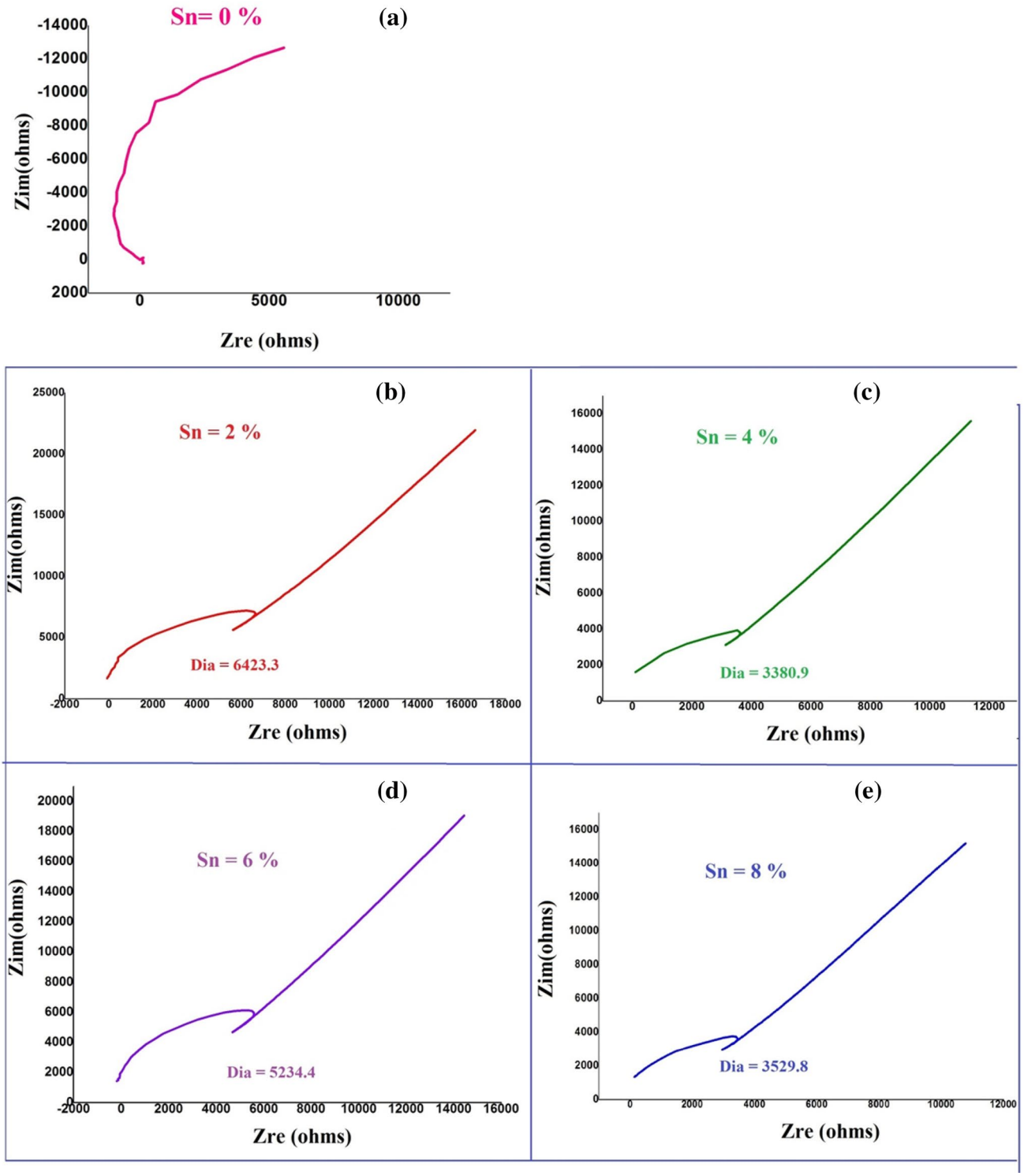

Fig. 7 Nyquist plot for Sn:ZnS nanoparticles

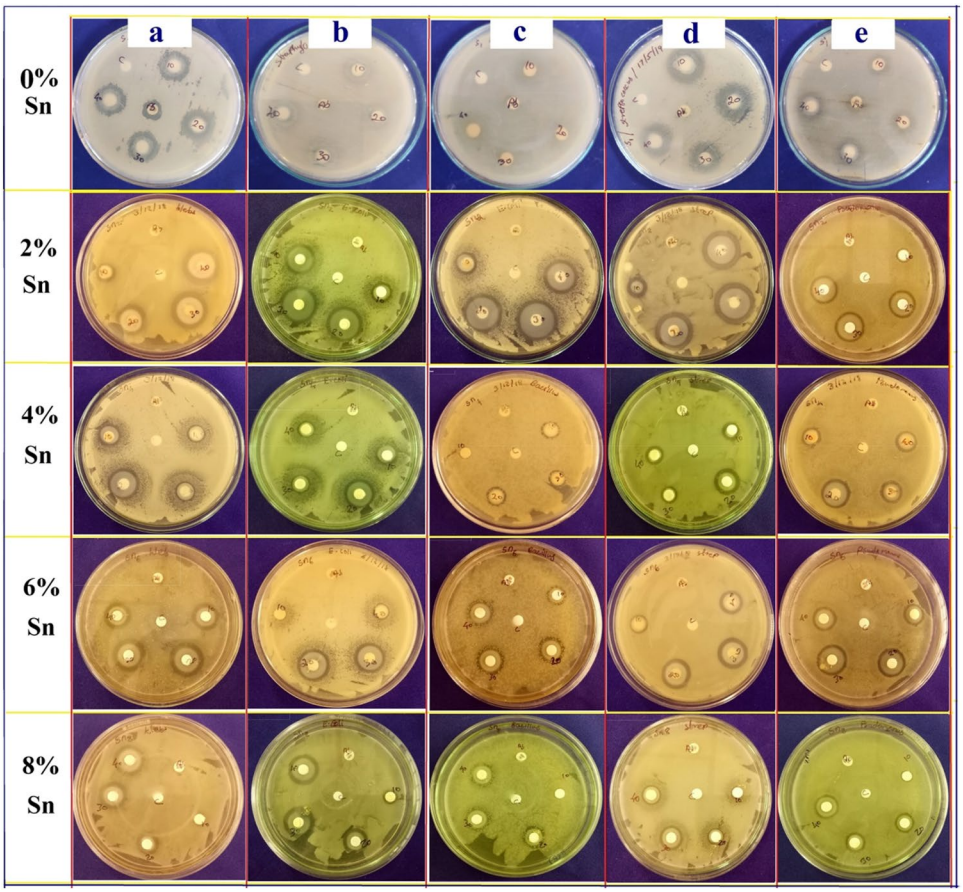

Fig. 8 Antibacterial studies of $Zn_{1-x}Sn_xS$ ($x = 0$, 0.02, 0.04, 0.06 & 0.08) nanoparticles

4 Conclusion

The Sn-doped ZnS nanoparticles were successfully synthesized for different concentrations of Sn from 0 to 8%. Sn-substituted ZnS QDs possessed cubic crystal structure and doping did not alter the host lattice. XRD results showed that particles size was gradually reduced due to Sn addition. TEM results showed the agglomeration of small-sized particles. UV absorption intensity of Sn-doped samples was raised and red shifted. Optical band-gap values were gradually reduced and quantum confinement effect was dominated by crystalline parameters change due to doping. PL emission was occurred in the UV region and no other visible light emission was received due to Sn incorporation. Since absorption was increased, the Sn-doped ZnS QDs will be useful in optoelectronic device fabrication and also as a buffer material in solar energy conversion modules. From electrochemical analysis, these were confirmed that 4% Sn doping was suitable to enhance catalytic activity and Sn-doping value 2% as best for energy-related electrical material applications. Antibacterial activity was enhanced and larger inhibition was occurred on Sn = 6% in *K. pneumonia*, *B. thuringiensis*, *S. aureus,* and *P. aureus*. Pure ZnS nanoparticles exhibited higher inhibition on *E. coli*. Hence, these materials can be chosen as antibacterial agent and it may be useful in food preserving industries.

Table 3 Antibacterial analysis of Sn-doped ZnS QDs with different doping concentrations

Cultures	Composition of Sn (%)	Zone inhibition diameter in millimeter			
		10 µg/ml	20 µg/ml	30 µg/ml	40 µg/ml
Klebsiella pneumonia	0	18	16	16	16
	2	10	14	12	11
	4	10	14	12	11
	6	16	19	19	16
	8	9	11	18	17
Escherichia coli	0	20	20	16	16
	2	13	17	11	11
	4	13	17	11	11
	6	Nil	17	17	10
	8	10	13	19	18
Bacillus thuringiensis	0	–	–	–	–
	2	Nil	11	10	10
	4	Nil	11	10	10
	6	11	14	16	14
	8	Nil	12	13	13
Staphylococcus aureus	0	10	10	13	13
	2	11	15	10	10
	4	11	15	10	10
	6	10	16	18	14
	8	Nil	10	14	12
Pseudomonas aureus	0	10	12	10	10
	2	11	16	12	12
	4	11	16	12	12
	6	13	17	16	15
	8	8	11	12	14

References

1. C.J. Murphy, Anal. Chem. **74**, 520A (2002)
2. J. Jie, W. Zhang, I. Bello, C.Z. Lee, S.T. Lee, Nano Today. **5**, 313 (2010)
3. V. Ramasamy, K. Praba, G. Murugadoss, Spectrochim. Acta. A **96**, 963 (2012)
4. S. Ummartyotin, N. Bunnnak, J. Juntaro, M. Sain, H. Mauspiya, Solid State Sci. **14**, 299 (2012)
5. S. Horoz, Q. Dai, F.S. Maloney, B. Yakami, J.M. Pikal, X. Zhang, J. Wang, W. Wang, J. Tang, Phys. Rev. App. **3**, 024011 (2015)
6. H. Labiadh, K. Lahbib, S. Hidouri, S. Touil, T.B. Chaabane, Asian Pac. J. Trop. Med. **9**, 757 (2016)
7. T. Krishnakumar, N. Pinna, K. PrasannaKumari, K. Perumal, R. Jayaprakash, Mater. Lett. **62**, 3437 (2008)
8. M. Peiteado, Y. Iglesias, J.F. Fernandez, J. DeFrutos, A.C. Caballero, Mater. Chem. Phys. **101**, 1 (2007)
9. C.Y. Tsay, H.C. Cheng, Y.T. Tung, W.H. Tuan, C.K. Lin, Thin Solid Films **517**, 1032 (2008)
10. T. Prakash, R. Jayaprakash, C. Espro, G. Neri, J. Mater. Sci. **49**, 1776 (2014)
11. P. Mani, K. Manikandan, J. Joseph Prince, J. Mater. Sci. **28**, 13602 (2017)
12. R. Sangeetha, S. Muthukumaran, Ceramics Int. **42**, 5921 (2016)
13. V. Vadhana sharon, S. Muthukumaran, J. Mater. Sci. **29**, 14935 (2018)
14. K. Chaitanya Kumar, N. Madhusudhana Rao, S. Kaleemulla, G. Venugopal Rao, Phys. B. **522**, 75 (2017)
15. J.H. Wang, Y.-C. Liu, S.S.-J. Lee, M.-Y. Yen, Y.-S. Chen, J.-H. Wang, S.-R. Wann, H.-H. Lin, Clin. Infect. Dis. **26**, 1434 (1998)
16. E.B. Hirsch, V.H. Tam, J. Antimicrob. Chemother. **65**, 1119 (2010)
17. E. Helgason, O.A. Okstad, D.A. Caugant, H.A. Johansen, A. Fouet, M. Mock, I. Hegna, A.B. Kolsto, Appl. Environ. Microbiol. **66**, 2627 (2000)
18. S.Y.C. Tong, J.S. Davis, E. Eichenberger, T.C. Holland, V.G. Fowler, Clin. Microbiol. Rev. **28**, 603 (2015)
19. E. Gordanian, S. Jalali-Asadabadi, I. Ahmad, S. Rahimia, M. Yazdani-Kachoei, RSC Adv. **5**, 23320 (2015)
20. S.K. Mehta, S. Kumar, S. Chaudhary, K.K. Bhasin, M. Gradzielski, Nanoscale Res. Lett. **4**, 17 (2009)
21. G.P. Bodey, R. Bolivar, V. Fainstein, L. Jadeja, Rev. Infect Dis. **5**, 279 (1983)
22. J.B. Kaper, J.P. Nataro, H.L. Mobley, Nat. Rev. Microbiol. **2**, 123 (2004)
23. D. Chandran, L.S. Nair, S. Balachandran, K. Rajendra babu, M. Deepa, J Sol-Gel Sci. Technol. **76**, 582 (2015)
24. M. Mall, L. Kumar, J. Lumin. **130**, 660 (2010)
25. S. Ameen, M.S. Akhtar, H.K. Seo, Y.S. Kim, H.S. Shin, Chem. Eng. J. **187**, 351 (2012)
26. J. Duan, X. Huang, H. Wang, Q. Zhong, F. Sun, X. He, Mater. Chem. Phys. **106**, 186 (2007)
27. P. Sakthivel, S. Muthukumaran, J. Phys. Chem. Solids **120**, 183 (2018)
28. P. Sakthivel, S. Muthukumaran, Opt. Laser Technol. **103**, 109 (2018)

29. K. Prabhu, S. Kannan, J. Henry, G. Sivakumar, K. Mohanraj, J Sci. Technol. (WJST) **11**, 795 (2013)
30. N. Nripasree, N.K. Deepak, Mater. Sci. Eng. B **211**, 121 (2016)
31. P. Sakthivel, S. Muthukumaran, J. Mater. Sci. **28**, 8309 (2017)
32. R. Veerasubam, S. Muthukumaran, Mater. Res. Express **6**, 045006 (2019)
33. B.E. Sernelius, K.F. Berggren, Z.C. Jin, I. Hamberg, C.G. Granqvist, Phys. Rev. B **37**, 10244 (1988)
34. T. Prakash, R. Jayaprakash, C. Espro, G. Neri, J. Mater. Sci. **49**, 1776 (2014)
35. T. Matsumoto, H. Kato, K. Miyamoto, M. Sano, E.A. Zhukov, T. Yao, Appl. Phys. Lett. **8**, 1231 (2002)
36. P. Sakthivel, G.K.D. Prasanna Venkatesan, K. Subramaniam, P. Muthukrishnan, J. Mater. Sci. **30**, 11984 (2019)
37. B. Malinowska, M. Rakib, G. Durand, Solar Energy Mater. Solar Cells. **86**, 399 (2005)
38. P. Sakthivel, S. Muthukumaran, J. Inorg. Organomet. Polym. **26**, 563 (2016)
39. C. Ravi Dhas, A. Jennifer Christy, R. Venkatesh, S.K. Panda, B. Subramanian, K. Ravichandran, P. Sudhagar, A. Moses, J. Solid State Electrochem. **22**, 2485 (2018)
40. J. Ma, W. Shen, C. Li, F. Yu, Light reharvesting and enhanced efficiency of dye- sensitized solar cells based 3D-CNT/graphene counter electrodes. J Mater Chem A. **3**, 12307 (2018)
41. S.K. Swami, N. Chaturvedi, A. Kumar, N. Chander, V. Dutta, D.K. Kumar, A. Ivaturi, S. Senthilarasu, H.M. Upadhyaya, Phys. Chem. Chem. Phys. **16**, 23993 (2014)
42. W. He, H. Jia, J. Cai, X. Han, Z. Zheng, W.G. Wamer, J. Yin, J. Phys. Chem. C **120**, 3187 (2016)
43. V. Vadhana Sharon, S. Muthukumaran, Mater. Res. Express. **5**, 6 (2018)
44. M.Y. Jehad, N.D. Enas, J. Health Sci. **2**, 38 (2012)
45. B.V. Schwartz, T. Frank, R. Sandra, P. Sabine, C. Lars, L. Alexandros, F. Renate, L. Katharina, J. Ulrich Adv. Funct. Mater. **22**, 2376 (2012)